Altering ligand fields in single-atom sites through second-shell anion modulation boosts the oxygen reduction reaction

Jiayi Qin,[†,‖] Hui Liu,[†,‖] Peichao Zou,[†] Rui Zhang,[†] Chunyang Wang,[†] Huolin L. Xin*[†]

[†]Department of Physics and Astronomy, University of California, Irvine, Irvine, California 92697, United States

[‖]These authors contributed equally

KEYWORDS: ruthenium single atoms, second shell, anion modulation, oxygen reduction reaction, metal-air batteries

ABSTRACT: Single-atom catalysts based on the metal-N_4 moieties and anchored on carbon supports (defined as M-N-C) are promising for oxygen reduction reaction (ORR). Among those, M-N-C catalysts with 4d and 5d transition metal ($TM_{4d, 5d}$) centers are much more durable and not susceptible to the undesirable Fenton reaction, especially compared with 3d transition-metal-based ones. However, the ORR activity of these $TM_{4d, 5d}$-N-C catalysts is still far from satisfactory; thus far, there are few discussions about how to accurately tune the ligand fields of single-atom $TM_{4d, 5d}$ sites in order to improve their catalytic properties. Herein, we leverage single-atom Ru-N-C as a model system and report an S-anion coordination strategy to modulate the catalyst's structure and ORR performance. The S anions are identified to bond with N atoms in the second coordination shell of Ru centers, which allows to mediately manipulate the electronic configuration of central Ru sites. The S-anion-coordinated Ru-N-C catalyst delivers not only promising ORR activity but also outstanding long-term durability, superior to commercial Pt/C and most of the near-term single-atom catalysts. DFT calculations reveal that the high ORR activity is attributed to the lower adsorption energy of ORR intermediates at Ru sites. Metal-air batteries using this catalyst in the cathode side also exhibit fast kinetics and excellent stability.

INTRODUCTION

Highly efficient and robust catalysts towards oxygen reduction reaction (ORR) are a determinative component for fuel cells and metal-air batteries. Hitherto, Pt-based bulk materials (*e.g.*, Pt/C) have been widely investigated and commercialized as state-of-the-art ORR catalysts, owing to their sufficiently high reaction kinetics.[1,2] However, the large-scale application of Pt-based catalysts is impeded primarily by their rarity and high cost, since a considerable amount of catalyst is demanded.[3-6] Single-atom catalysts offer a tantalizing solution to lowering down the cost with maximized atomic utilization efficiency and tunable electronic properties.[7-11] Among these catalysts, atomically dispersed metals anchored on the nitrogen-doped carbon texture (M-N-C) hold particular promise owing to their dramatic catalytic performance towards ORR,[12-15] in which the planar four-coordinated configuration of metal-N_4 (M-N_4) moieties have been generally validated as the active sites.[14,16-19]

3d transition-metal (TM_{3d})-based M-N-C catalysts (M = Fe, Co, Ni, Mn, Cu, *etc*.) possess promising ORR activities, yet they suffer from the detrimental Fenton reaction even though many approaches to improve the selectivity for 4-electron transfer products have been attempted.[20-23] Thus far, 1) the formation of two-electron reaction products with lower efficiency (compared with the four-electron reaction product), as well as 2) the fast performance degradation due to the leaching of 3d transition metals have not been resolved. The reactive oxygen species of free radicals (such as hydroxyl radicals) generated by the Fenton reaction will also attack the polymer membrane in fuel cells, accelerating their failure.[24] These limitations compromise the low-cost benefits of TM_{3d}-N-C catalysts and impede their wide application in commercial fuel cells. In comparison, M-N-C catalysts based on 4d and 5d-transition-metal ($TM_{4d,5d}$) centers, particularly those with the stable arrangement of outer shell electrons, such as Ru and Ir, have displayed better long-term durability due to the negligible interaction between these $TM_{4d,5d}$ ions and hydrogen peroxide (*i.e.*, Fenton reaction).[23,25] Unfortunately, a remaining conundrum for these catalysts lies in unsatisfactory activity caused by the sluggish ORR kinetics, which is determined by the coordination and electronic structure of the active metal site.[23,25]

As a widely investigated $TM_{4d,5d}$-N-C electrocatalyst, atomically dispersed Ru-N-C catalysts have been generally identified to have a strong adsorption strength of ORR intermediates at Ru-N sites,[25,26] unfavorable for the desorption of ORR products. Therefore, lowering down the adsorption strength of

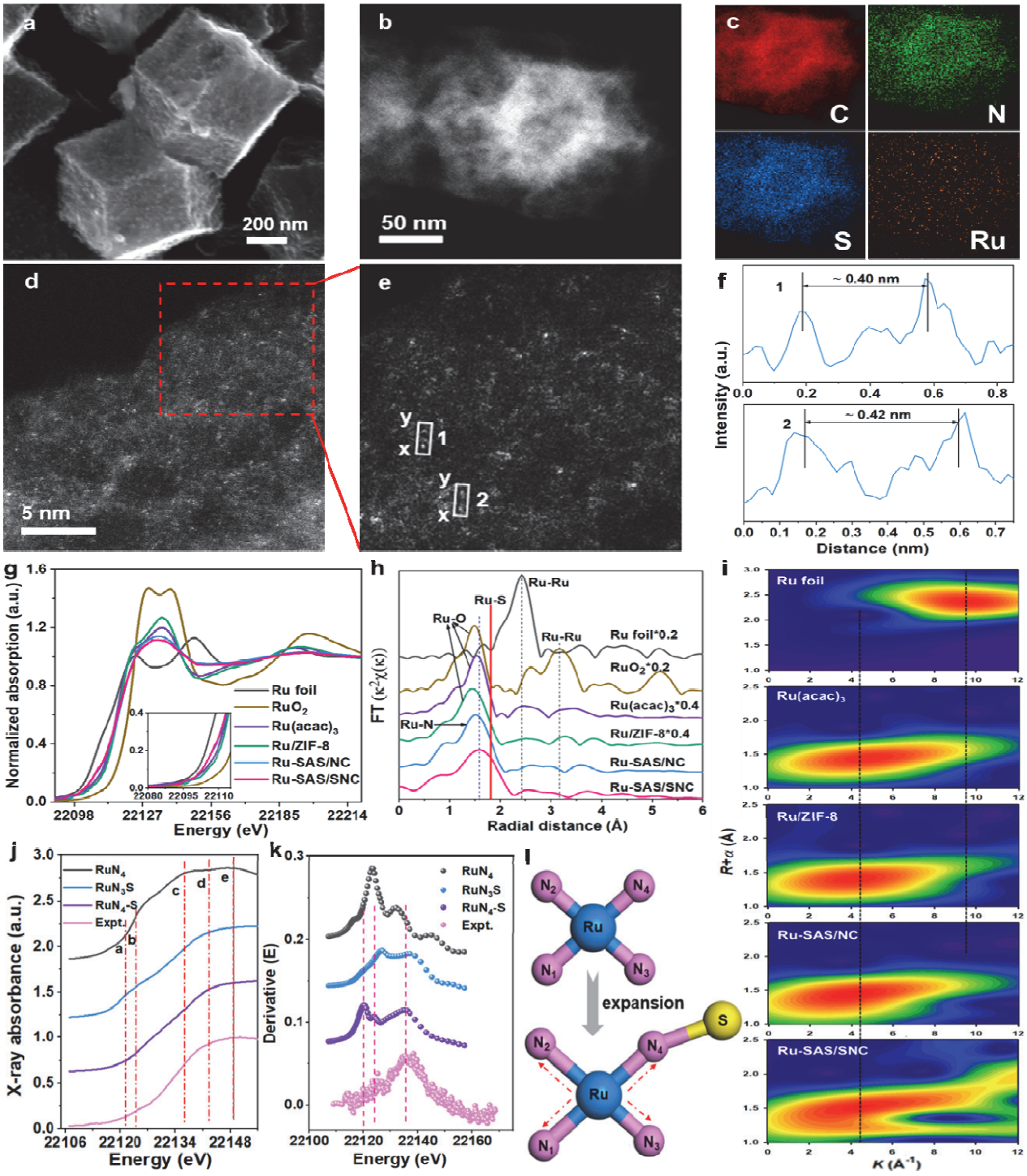

Figure 1. Morphology and atomic structure characterizations of Ru-SAS/SNC. (a) SEM, (b) HAADF-STEM and (c) EDS images of Ru-SAS/SNC, C (red), N (green), S (blue) and Ru (orange). (d) AC-HAADF-STEM image and (e) the magnified image of Ru-SAS/SNC. (f) The corresponding intensity profiles along the line X-Y in (e). (g) Experimental Ru K-edge XANES spectra of Ru-SAS/SNC and reference samples. (h) Fourier-transformed magnitude of the experimental Ru K-edge EXAFS signal of Ru-SAS/SNC, along with reference samples. (i) WT-EXAFS plots of Ru-SAS/SNC, Ru foil, $Ru(acac)_3$, Ru/ZIF-8, and Ru-SAS/NC, respectively. (j) Comparison between the experimental Ru K-edge XANES spectrum of Ru-SAS/SNC and the theoretical spectra calculated for the depicted structure. (k) Comparison of Ru K-edge XANES spectra between the experimental derivation (E) of Ru-SAS/SNC and the theoretical results calculated for the depicted structure. (l) Schematic atomic model of Ru-N bond length changes before and after S introduction. Color scheme: blue for Ru, yellow for S, pink for N, and grey for C.

ORR intermediates at Ru-involved reactive sites would contribute to accelerating the ORR kinetics and enhancing the ORR activity. In molecular catalysis, one effective strategy for improving the catalyst's activity is to change the ligand environment by modulating the active metal site with anions (S, P, *etc*.) with different electronegativities, and thus the intermediates' binding energies and transition kinetics can be optimized through the withdrawing/donating effects of these exotic anions.[27-33] It was reckoned therefore that exploring anion-coordinated Ru-N-C electrocatalysts would also be effective to modulate the adsorption strength of ORR intermediates at the active sites to further optimize the ORR activity, which however has been rarely studied, let alone the accurate orientation of coordination sites for the anions as well as their definitive influence on the ORR performance.

Here, we report a S-anion-coordinated atomically dispersed Ru-N-C catalyst (Ru-SAS/SNC) for ORR, where S anion is located at the second shell and directly coordinated with N in the Ru-N_4 moiety (denoted as RuN_4-S). The coordination structure of Ru-SAS/SNC was unveiled by synchrotron-based X-ray absorption spectroscopy (XAS) together with density functional theory (DFT) calculations, in which the immigrated S at the second shell can tailor the d-orbital electronic structure of central Ru to reduce the energy barrier of ORR-related species at Ru sites within the RuN_4-S, thus promoting the ORR activity. The resultant Ru-SAs/SNC catalyst exhibits excellent ORR activity with a positive half-wave overpotential ($E_{1/2}$) of 0.861 V (*vs.* reversible hydrogen electrode (RHE)) and high kinetic current density (J_k) of 101.7 mA cm^{-2} at 0.80 V, which surpasses that of Pt/C ($E_{1/2}$ = 0.853 V *vs.* RHE, J_k = 19.3 mA cm^{-2}) and approaches record-level among previously reported single-atom catalysts. Remarkably, Ru-SAS/SNC also delivers extraordinary long-term durability with only 24 mV negative shift in $E_{1/2}$ after 30000 cycles. Multifarious metal-air (Zn-air, Al-air, and Li-air) battery tests reveal that the batteries based on Ru-SAS/SNC generally present superior discharge performances to those based on commercial Pt/C, further demonstrating the versatile merits of Ru-SAS/SNC in the field of energy storage and conversion.

RESULTS AND DISCUSSION

Morphology and coordination structure characterizations of Ru-SAS/SNC. The Ru-SAS/SNC was synthesized via a hydrothermal-and-pyrolysis combined strategy (Figure S1). Firstly, $Ru(acac)_3$ and Zn^{2+} were mixed with 2-methylimidazole at 120 ℃ to enable the self-assembly process, after which Ru ions were trapped in zeolitic imidazolate frameworks (ZIF-8) to form the Ru/ZIF-8 intermediates. Here, ZIF-8 was employed as the molecular-scale cages to in-situ trap and encapsulate metal precursors during crystallization. Subsequently, Ru/ZIF-8 and sulfur powder were dispersed in a mixture solvent of carbon disulfide and ethanol, then dried by stirring under low-temperature heating, ensuring the attachment of sulfur particles onto the surface of Ru/ZIF-8 (S/Ru/ZIF-8). Finally, Ru-SAS/SNC was obtained by pyrolyzing S/Ru/ZIF-8 at 950 ℃ under Ar atmosphere. During the pyrolyzation process, sulfur will penetrate into the ZIF-8 frameworks and the inner metallic zinc will be evaporated.[23,34] Meanwhile, it will also allow the *in-situ* generation and immobilization of Ru single atoms on carbonized skeletons, induced by the strong metal anchoring ability of N atoms and the space-confinement effect of micropores within the skeletons. Control samples, NC (N-doped carbon substrate), SNC (S-coordinated and N-doped carbon substrate), Ru-SAS/NC (without coordinated-S anions), Ru-SAS//SNC (no connection between S and Ru) were also prepared through a similar method (Supporting Information). Noted that the optimized Ru-SAS/SNC sample was obtained with a $m_{sulfur\ powder}$: $m_{Ru/ZIF-8}$ ratio of 1:20, which was determined according to the ORR performance test (Figure S2). Such optimized Ru-SAS/SNC sample was thereafter used for further characterization and electrochemical evaluations, unless stated otherwise.

The complete carbonization of the precursor was verified by the appearance of typical carbon peaks at around 25° for (002) facet and 44° for (100)/(101) facet, and the absence of well-maintained crystalline peaks for ZIF-8 derived carbon frameworks in X-ray diffraction (XRD) patterns (Figure S3). Note that there are no characteristic diffraction peaks of metallic crystalline Ru, implying the atomically dispersed Ru incorporation with N in the carbon skeleton.[25] The Raman spectra (Figure S4) show that the intensity ratio between D-band (≈1337 cm^{-1}, defective carbon) and G-band (≈1586 cm^{-1}, graphitic carbon) for Ru-SAS/SNC was close to 1.02, which is larger than those of NC, SNC, and Ru-SAS/NC samples, signifying the existence of more defects in Ru-SAS/SNC.[35,36] According to the Field-emission scanning electron microscopy (FESEM) and transmission electron microscopy (TEM) experiments, it reveals that the rhombododecahedron shape of ZIF-8 nanocrystals can be retained during the *in-situ* $Ru(acac)_3$ encapsulation and following the pyrolysis process under 950 °C (Figure S5). The uneven surface with plenty of bumps and the highly open porous structure in the finally obtained Ru-SAS/SNC is beneficial for a large surface area, abundant active sites, and accelerated mass-charge transportation.[28] Sulfur powder can be adsorbed on the surface of Ru/ZIF-8 architecture by dispersing in carbon disulfide-ethanol mixed solution, with nonuniform particle sizes of several nanometers to hundreds of nanometers (Figure S6 and S7). In the pyrolysis process, porous carbon frameworks could be further etched by the gradual permeation of sulfur (Figure 1a, b, and Figure S8). However, the excessive damage and collapse of the polyhedral structure were prevented, attributed to the homogenous dispersion of $Ru(acac)_3$ within ZIF-8 and *in situ*-stabilization of Ru atoms by N coordination sites during ZIF pyrolysis.[29,36] BET specific surface area and porosity distributions also indicate that Ru-SAS/SNC possesses a higher surface area and larger porous structure than Ru-SAS/NC (Figure S9 and Table S1), which result from the etched porous structure after S participation in Ru-SAS/SNC. Moreover, no Ru nanoparticles or clusters were detected in High-resolution TEM (HRTEM) and high-angle annular dark-field scanning TEM (HAADF-STEM) images (Figure S10a, b). Energy-dispersive X-ray (EDX) analysis in HAADF-STEM manifests homogeneous distribution of C, N, S, and Ru elements within Ru-SAS/NC and Ru-SAS/SNC (Figure 1c, Figure S10c, and Figure S11a-c). The Ru mass percentage content in Ru-SAS/SNC is determined as 0.5 wt.% according to the inductively coupled plasma mass spectrometry (ICP-MS) measurement (Table S2). Obviously, in the aberration-corrected HAADF-STEM (AC-HAADF-STEM) images (Figure 1d, e, Figure S11, and Figure S12), monodispersed Ru single atoms could be identified by isolated bright dots in both Ru-SAS/NC and Ru-SAS/SNC samples. Additionally, the space measured between two Ru atoms

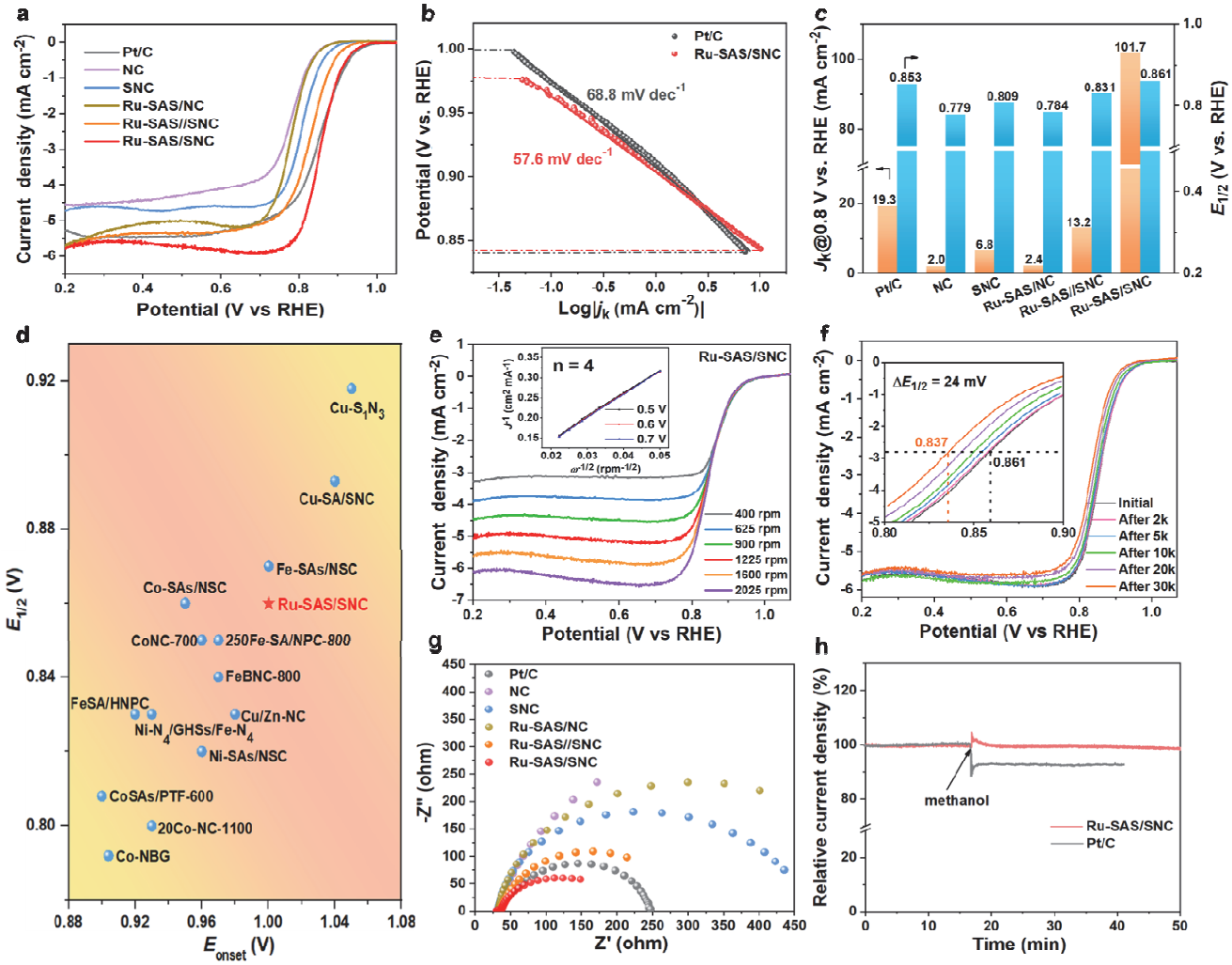

Figure 2. ORR activity of Ru-SAS/SNC. (a) Polarization curves for Ru-SAS/SNC and the references tested in O_2-saturated 0.1 M KOH solution with a scanning rate of 5 mV s^{-1} at 1600 rpm. (b) Tafel slopes for Ru-SAS/SNC and Pt/C. (c) The contrast between Ru-SAS/SNC and the references for J_k (0.80 V) and $E_{1/2}$. (d) Comparison of the E_{onset} and $E_{1/2}$ values between Ru-SAS/SNC and the catalysts reported recently. (e) The polarization curves of Ru-SAS/SNC at different rotating speeds. The insert is the corresponding K-L curves at different potentials. (f) The long-term durability tests of Ru-SAS/SNC. The inset is the magnified images. (g) Nyquist plots of electrochemical impedance spectra of Ru-SAS/SNC and the references. (h) The *i-t* curves of Ru-SAS/SNC and commercial Pt/C before and after the addition of 1.0 M methanol.

exceeds 0.4 nm (Figure 1f), which consolidates the isolated atom feature of Ru existed in Ru-SAS/SNC.[37]

To accurately distinguish the chemical and electronic states of atomically dispersed Ru species, X-ray photoelectron spectroscopy (XPS), X-ray absorption energy near-edge structure (XANES), and extended X-ray absorption fine structure (EXAFS) spectroscopy were utilized. The survey XPS spectrum of Ru-SAS/SNC (Figure S13a) demonstrates the coexistence of C, N, O, S, Zn, and Ru elements. Residual Zn content in Ru-SAS/SNC is quantified to be as low as 0.11 at.%, which would exert negligible influence on catalytic performance.[29,38] Since Ru 3d photoelectrons signal overlaps with that of C 1s from carbon substrates (Figure S13b), we adopted the Ru 3p XPS spectra to avoid strong interference.[26] The normalized C 1s spectra of Ru-SAS/SNC (Figure S14a) could be deconvoluted into C-C/C=C bonds (284.8 eV), C=C-N bonds (285.9 eV), and N-C=N bonds (289.4 eV), respectively.[34] Meanwhile, the N 1s XPS spectrum of Ru-SAS/SNC (Figure S14b) exhibits four peaks at binding energies of 398.2, 398.9, 400.3, and 401.2, which can be assigned to pyridinic N, N-S bonding, pyrrolic N, and graphitic N, respectively.[39,40] In comparison, only three peaks belonging to pyridinic N, pyrrolic N, and graphitic N can be found in Ru-SAS/NC without characteristic peaks of the N-S bond (Figure S15). S 2p XPS spectrum of Ru-SAS/SNC (Figure S14c) can be deconvoluted into three peaks: S $2p_{3/2}$ (163.9 eV), S $2p_{1/2}$ (165.0 eV), and sulfate species (C-SO_x).[31,41] The absence of the characteristic peak of metal-S bond implies exotic S atoms tend to bond to surrounding N atoms, not directly to the central Ru atoms. Regarding the Ru 3d XPS spectrum of Ru-SAS/SNC (Figure S14d), only two weak peaks for Ru $2p_{3/2}$ (~ 462.5 eV) and Ru $2p_{1/2}$ (~ 485.0 eV) can be observed, which can be poorly leveraged to identify the oxidation state of Ru atoms. This is because Ru photoelectronic signals may be attenuated due to the encapsulation of a thick rhombic dodecahedron framework

with a size of ~ 200 nm.[38] Notably, N 1s and Ru 3p XPS peaks of Ru-SAS/SNC shift toward a lower binding energy direction compared to those of Ru-SAS/NC without S source (Figure S16), suggesting a partial electron transfer from S atoms to N atoms and then to central Ru sites.

To probe the electronic and atomic states of C, N, and S in Ru-SAS/SNC, synchrotron-based soft XANES was first carried out by collecting the surficial information using the total electron yield (TEY) mode. As shown in Figure S17a, the C K-edge XANES spectra present four spectroscopic features, which could be assigned to the dipole transition of the C 1s core electron into the π^*(peak a, C=C), π^*(peak b_1 and peak b_2, C-N/S), and σ^* (peak c, C-C) antibonding orbitals.[29] Compared to the NC sample, the peak b_1 and peak b_2 of SNC and Ru-SAS/NC slightly shift toward lower binding energies after incorporating S or Ru into the carbon matrix. However, in contrast to Ru-SAS/NC, a mild deviation toward higher binding energy is found on the peak b_1 and peak b_2 for Ru-SAS/SNC, implying a valid sulfur-modification in Ru-N_4 moiety. In N K-edge XANES spectra (Figure S17b), the d_1, d_2, and e peaks are assigned to pyridinic N and pyrrolic N, respectively, and peak f denotes graphitic N.[29,30,34] When compared with the NC sample, the peak d_1 in Ru-SAS/NC shifts to the lower energy direction, suggesting the strong chemical coordination between pyridinic N and Ru sites, corresponding to Ru-N-C bonding in Ru-SAS/NC. When comparing Ru-SAS/NC with Ru-SAS/SNC, peak d_1 presents a continuous migration towards the lower energy direction in Ru-SAS/SNC, signifying the partial electron transfer from S to N atoms. Furthermore, the valence of S was investigated by the S K-edge XANES spectra (Figure S18), from which we can see the Ru-SAS/SNC possesses a slightly positive shift in the K-edge position compared with SNC, which is ascribed to the electron transfer from S to N then to Ru atoms that leads to a S-N-Ru coordination. These results are consistent with the XPS analysis above.

Hard X-ray absorption spectroscopy (hXAS) measurement was also carried out to evaluate the local electronic and atomic structure around Ru centers, in which the atomic-site structures around the photo-absorber could be better identified by the X-ray absorption energy near-edge structure (XANES) spectroscopy that captures the information about the three-dimensional arrangement of the atoms.[26,38] As illustrated in Figure 1g, the absorption energy edges and the white line intensities of Ru-SAS/SNC, Ru-SAS/NC, and Ru-ZIF-8 are situated between those of Ru foil and RuO_2 in the Ru K-edge XANES spectra, elucidating the partial oxidation of Ru with valence states of 0 to +4. In addition, the absorption edge positions of Ru-SAS/SNC and Ru-SAS/NC are comparable to those of $Ru(acac)_3$ and Ru-ZIF-8, indicating the valence state of Ru-SAS is close to +3. It can also be observed that the absorption energy and white line peak intensity of Ru-SAS/SNC are slightly lower than those of Ru-SAS/NC, which exemplifies a lower oxidation state of Ru-sites in Ru-SAS/SNC than in Ru-SAS/NC, originating from the electron migration from S to Ru. This result is consistent with the results of XPS. It is well known that the pre-edge intensities are directly proportional to the coordination deviation of the centrosymmetric photo-absorbers[26,42] and thus the higher intensity of the pre-edge peak in Ru-SAS/NC and Ru-SAS/SNC compared to $Ru(acac)_3$ and Ru-ZIF-8, demonstrates that distorted octahedral coordination is adopted for Ru atoms in isolated reaction sites-containing samples.[38]

To further confirm the atomic Ru distribution and unveil the precise coordination environment in Ru-SAS/SNC, normalized Fourier transform of the extended X-ray absorption fine structure (FT-EXAFS) spectroscopy was employed. In the FT-EXAFS curves (Figure 1h), unlike Ru-O bonds located at ~1.45 Å in RuO_2, $Ru(acac)_3$, and Ru/ZIF-8, the identified major peak in Ru-SAS/SNC is located at ~1.59 Å, which is slightly larger than that of the Ru-N peak (~1.50 Å) in Ru-SAS/NC and shorter than that of Ru-S bond appearance (~1.81 Å).[43] Considering that the characteristic peak's location of Ru-SAS/SNC is more similar to that of Ru-N and significantly different to that of Ru-S bonds, it is reasonable to deduce the dominant bonding pairs with central metal atoms is Ru-N rather than Ru-S in Ru-SAS/SNC. The main peak of Ru foil is situated at ~2.41 Å, corresponding to the Ru-Ru coordination. However, there is no such peak in the Ru-SAS/SNC sample, which confirms the presence of isolated ruthenium sites, consistent with the above STEM results. Furthermore, wavelet transformed (WT) EXAFS analysis, featured with simultaneous resolution in both *k* and *R* spaces, was used to distinguish atomic species of backscattering atoms, since some important information is lost in the magnitude of the Fourier-transformed signal.[44-46] As shown in Figure 1i, WT contour plots of Ru metal foil show an intensity maximum at 9.50 $Å^{-1}$, attributed to metallic Ru-Ru coordination. The WT contour plots of $Ru(acac)_3$ and Ru/ZIF-8 display the intensity maximum at 4.75 $Å^{-1}$ and 4.40 $Å^{-1}$, respectively, which could be ascribed to Ru-O bonding. Whereas, only one intensity maximum at 4.05 $Å^{-1}$ was detected in the WT contour plots of Ru-SAS/SNC, and the *k*-space value is very close to that of Ru-N contribution (3.96 $Å^{-1}$) in Ru-SAS/NC, validating that Ru exists as atomically monodispersed centers without metal-derived Ru structures in Ru-SAS/SNC.[25]

To verify whether sulfur is attached to peripheric N or nuclear Ru atoms, optimized DFT calculation models were established to execute XANES simulation (Figure S19). Among the simulated Ru K-edge XANES spectra based on the models of RuN_4, RuN_3S, and RuN_4-S moieties embedded in a graphene sheet (Figure 1j), the simulated spectrum of RuN_4-S moieties was found well reproduced with the experimental spectrum; in contrast, the predicted XANES profiles of RuN_4 and RuN_3S moieties are distinct to the experimental XANES profile of Ru-SAS/NC, particularly in near-edge features (a-e). Moreover, the characteristic signals of the experimental *E*-space derivation of Ru-SAS/SNC only cohere with predicted ones of RuN_4-S moiety (Figure 1k). Therefore, as expected, S atoms are bonded with N atoms in the second shell rather than central Ru atoms (Figure S19c), which allows indirect electronic regulation of Ru nucleus from the second shell, coinciding with the above XPS and EXAFS analysis. The bonding between S and N atoms thereafter initiates a slight asymmetrical expansion of the original Ru-N bonds (Figure 1l). Detailed bond length changes are displayed in Table S3. In addition, the EXAFS fitting was also operated to further extract the structure parameters (Figure S20),[43] and the fitting results revealed that the dominant coordination peak of Ru-SAS/SNC corresponds to four-coordinate Ru centers in the form of Ru-N_4 configuration. Compared with the case in Ru-SAS/NC, the mean Ru-N bond length of Ru-SAS/SNC (1.886 Å) is slightly increased, due to the incorporation of S atoms into the Ru-N_4 species.

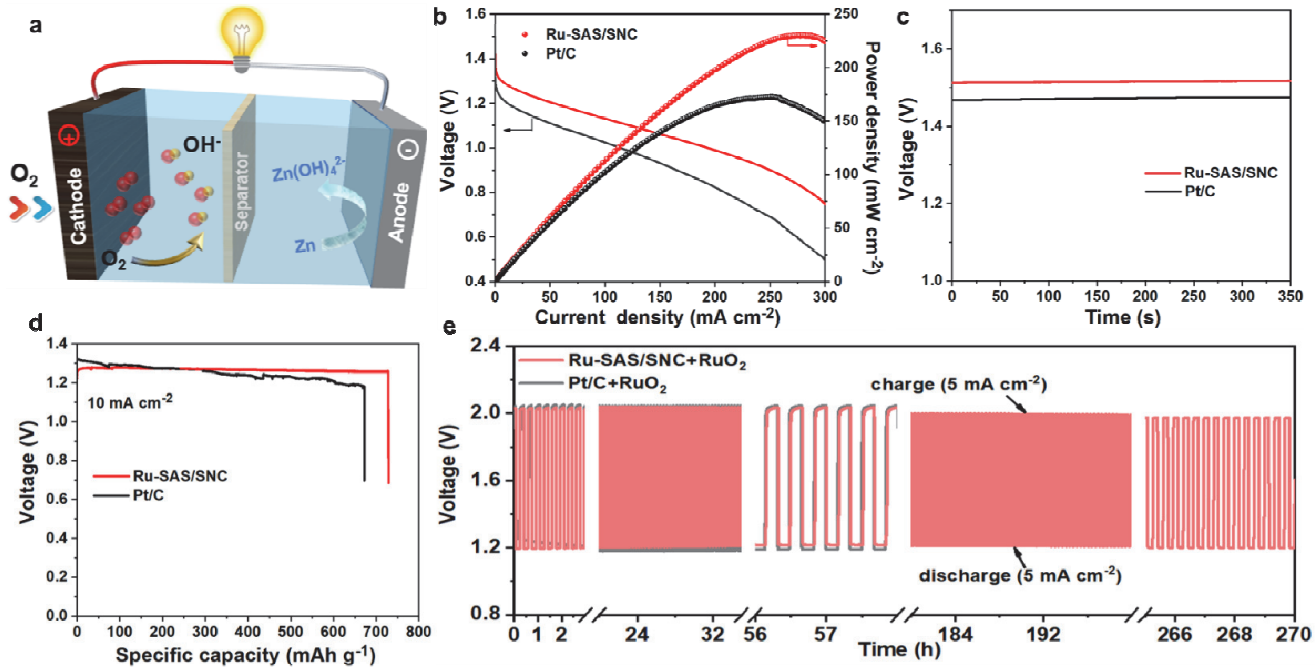

Figure 3. Zn-air battery performance using Ru-SAS/SNC. (a) Schematic setup diagram of Zn-air battery. (b) Discharge polarization curves and power density plots of Ru-SAS/SNC and Pt/C-based Zn-air batteries. (c) The open-circuit voltage plots of Zn-air batteries assembled with Ru-SAS/SNC and Pt/C. (d) Specific capacity by mass normalization at a current density of 10 mA cm^{-2}. (e) Galvanostatic charge/discharge cyclic curves of the Zn-air batteries at 5 mA cm^{-2} with a duration of 1200 s per cycle in 6.0 M KOH.

Based on the above analysis, we can conclude that the coordination structure of Ru-SAS/NC involves a Ru central atom surrounded by four nitrogen atoms in the first shell, with one sulfur atom replacing the position of carbon atoms in the second coordination sphere. Such coordination structure can readily trigger the electron transfer from S to N and then to center atoms due to the relatively high electron affinity of N, which could consequently increase the electron density of metal ions and thereby lower the intermediate adsorption free energy.[27,31] If S atoms are attached to the center metal ions at the first shell, the electrons around metal ions transfer to S atoms, leading to more intensive intermediates adsorption on reactive sites,[27,28] unfavorable for ORR.

ORR Electrocatalytic Performance of Ru-SAS/SNC. The ORR electrocatalytic performance of Ru-SAS/SNC was investigated in O_2-saturated 0.1 M KOH electrolyte using a typical three-electrode device calibrated by the reversible hydrogen electrode (RHE). Cyclic voltammetry (CV) curves of Ru-SAS/SNC exhibit characteristic cathodic peaks of ORR in O_2-saturated solution (Figure S21). To properly ascertain the influence of metal species, 0.01 M KSCN was injected into the electrolyte prior to the polarization scan.[35] Affected by the SCN^- coordination and blockage of Ru sites, apparent attenuated E_{onset}, $E_{1/2}$, and limited current density are presented in Ru-SAS/SNC after adding KSCN, implying the single-atomic Ru site is the main direct active center of ORR. The linear sweep voltammetry (LSV) polarization curves of different catalysts are presented in Figure 2a, in which Ru-SAS/SNC delivers the best ORR performance over its counterparts. Specifically, Ru-SAS/SNC demonstrates not only a high onset potential (E_{onset}) of 0.998 V (*vs.* RHE) comparable with Pt/C (1.00 V *vs.* RHE), but also the most positive half-wave potential ($E_{1/2}$) at 0.861 V (*vs.* RHE) that even surpasses that of Pt/C (0.853 V *vs.* RHE). In addition, the diffusion limited currents of NC and SNC are lower than those of other samples, which may be caused by the 2e pathway with more H_2O_2 production. Regarding the Ru single atoms-contained catalysts (*i.e.*, Ru-SAS/SNC, Ru-SAS//NC, and Ru-SAS/SNC), the limit diffusion current platforms are not ideally flat, possibly due to the locally inhomogeneous oxygen diffusion and gas absorption on the porous catalyst surface that covers the active sites.[47-49]

It is generally known that a smaller Tafel slope reflects an accelerated ORR reaction kinetics.[50-52] In Figure 2b, the Tafel slope is 57.6 mV dec^{-1} for Ru-SAS/SNC catalyst, which outperforms that of Pt/C (68.8 mV dec^{-1}), suggesting the smaller energy barrier to form the oxygen intermediates and the faster kinetic rate on Ru-SAS/SNC reaction surface.[53] Detailed catalytic performance derived from the LSV curves of all samples is summarized in Figure 2c. Among all samples, Ru-SAS/SNC possesses the optimal ORR activity with the uppermost $E_{1/2}$ and kinetic current density (J_k = 101.7 mA cm^{-2}), which is 5.3-fold as large as that of commercial Pt/C (J_k = 19.3 mA cm^{-2}). Notably, Ru single atoms-contained catalysts (*i.e.*, Ru-SAS/SNC, Ru-SAS/NC, and Ru-SAS//SNC) generally display both high $E_{1/2}$ and J_k compared to inornate NC ($E_{1/2}$ = 0.779 V, J_k = 2.0 mA cm^{-2}) and SNC ($E_{1/2}$ = 0.809 V, J_k = 6.8 mA cm^{-2}) frameworks derived from ZIF-8, indicating the crucial role of isolated Ru atoms as the real ORR reaction sites instead of N-C or S-N-C sites. Among the Ru single atoms-contained catalysts, Ru-SAS/SNC presents the highest $E_{1/2}$ and J_k values, better than Ru-SAS/NC comprised of Ru-N-C bonding ($E_{1/2}$ = 0.784 V, J_k = 2.4 mA cm^{-2}) and Ru-SAS//SNC comprised of separated Ru-N and S-N coordination ($E_{1/2}$ = 0.831 V, J_k = 13.2 mA cm^{-2}), proving the improvement of intrinsic ORR activity of central Ru sites after the creation

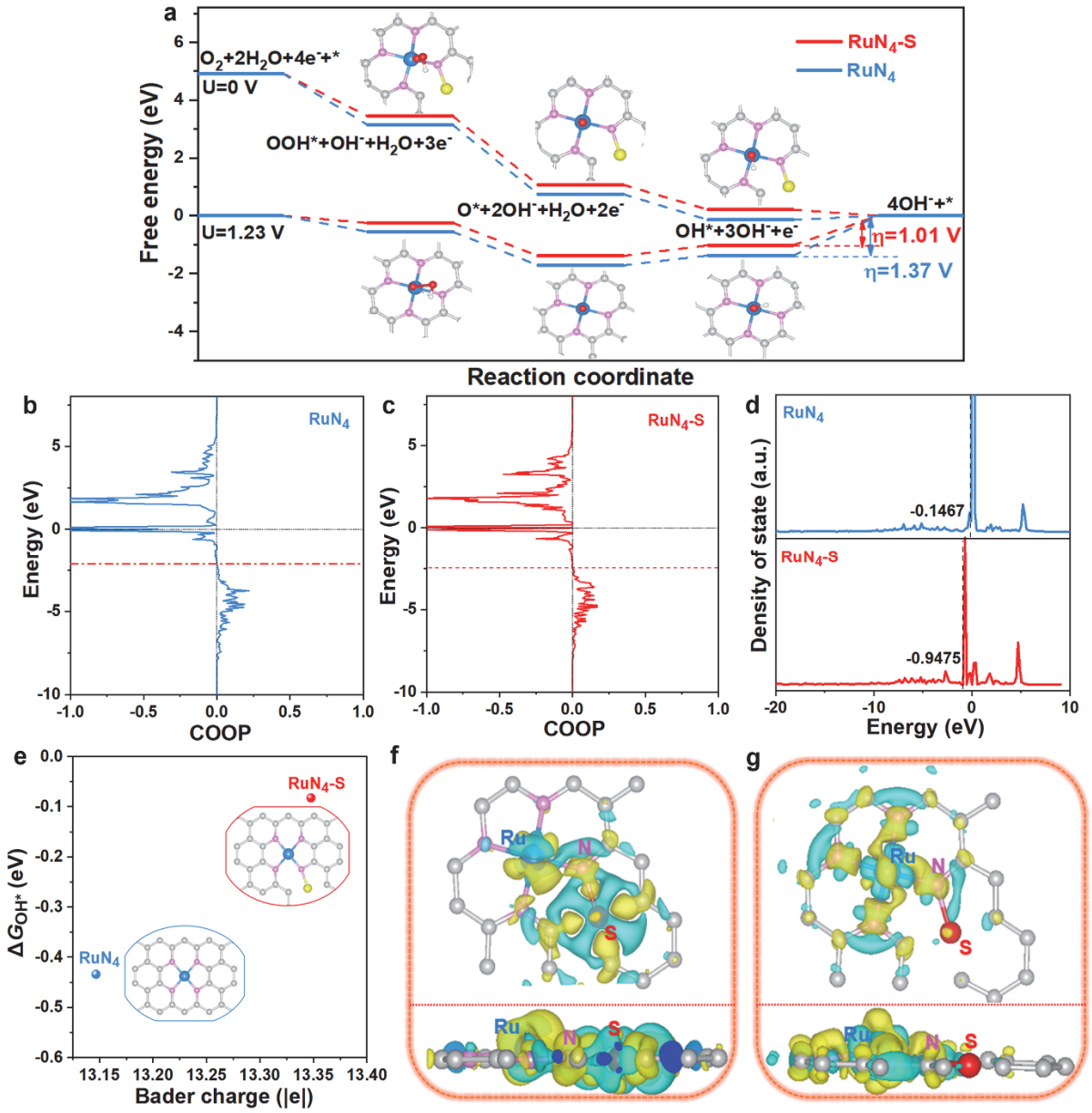

Figure 4. ORR catalysis mechanism of Ru-SAS/SNC. (a) Free-energy diagram for ORR process on RuN_4 and RuN_4-S moieties at the equilibrium potentials of U = 0 V and U = 1.23 V in the alkaline. Insert: The corresponding schematic models of samples. Color scheme: blue for Ru, yellow for S, pink for N, and grey for C. (b) Crystal orbitals overlap population (COOP) charts of RuN_4 moiety and (c) RuN_4-S moiety. (d) d-band centers of RuN_4 and RuN_4-S moieties. (e) Relationship between Bader charge and OH^* binding energy of single-atom Ru in RuN_4 and RuN_4-S, respectively. Insert: The corresponding schematic models of samples. Color scheme: blue for Ru, yellow for S, pink for N, and grey for C. Charge density difference of (f) S as the target and (g) Ru as the target in RuN_4-S moiety. Color scheme: blue for Ru, red for S, pink for N, and grey for C. Yellow regions indicate charge accumulation, while cyan regions indicate charge depletion.

of Ru-N-S conjunction. Moreover, the intrinsic ORR activity, namely ORR specific activity and mass activity, was further evaluated by normalizing the kinetic current at 0.8 V (*vs.* RHE) with respect to the BET surface area and Ru quality of Ru-SAS/NC and Ru-SAS/SNC catalysts (Table S4). The S-coordinated catalyst (Ru-SAS/SNC) displays considerably enhanced specific activity (SA) and mass activity (MA) compared to the Ru-SAS/NC sample, intuitively clarifying the influence of S introduction on the intrinsic activity of Ru sites. Additionally, the ORR activity obtained for Ru-SAS/SNC in this work is superior to those of most near-term reported single atoms-based electrocatalysts (Figure 2d and Table S5).

Apart from the ORR catalytic activity, Koutecky-Levich (K-L) plots originated from LSV curves at different rotating speeds (Figure 2e) were further utilized to evaluate the catalytic selectivity.[54,55] A direct four-electron ORR pathway is cal-

culated for Ru-SAS/SNC from the slope of the K-L plots under different potentials. Moreover, rotating ring-disk electrode (RRDE) measurements were conducted to calculate the electron transfer number (n) and peroxide yields (H_2O_2%) (Figure S23).[25] Clearly, Ru-SAS/SNC shows a very low H_2O_2 yield (< 5%) and its n value fluctuates between 3.88 and 3.98 at a potential range of 0.2-0.8 V (*vs*. RHE), consistent with the results obtained by K-L plots. The long-term durability test through repeated potential cycling in the range of 0.6 to 0.95 V (*vs.* RHE) shows that only 24 mV loss in $E_{1/2}$ was found on Ru-SAS/SNC after 30000 continuous cycles (Figure 2f), even superior to that of Pt/C (43 mV, Figure S24). Moreover, the chronoamperometric *i-t* measurement shows there is no appreciable current change during the 70 h test for Ru-SAS/SNC, outperforming Pt/C as well (Figure S25). The HAADF-STEM images (Figure S26) reveal that, after the durability test, Ru-SAS/SNC can still maintain its original morphology with isolated bright dots of single Ru atoms retained on the substrate, which could be attributed to the eminent anchoring effect of coordinated anions that effectively suppresses Ru leaching. As shown in the electrochemical impedance spectra (EIS), the smaller semicircle diameter of Ru-SAS/SNC implies the faster charge transfer (Figure 2g). In the frequency range of 0.1 Hz to 10^6 Hz, the EIS plots of the composite catalysts (Ru-SAS/SNC, Ru-SAS//NC, and Ru-SAS/SNC) are close to a quarter circle rather than an ideal semicircle, possible due to the faster charge transfer within these catalysts so that the mass transfer-controlled process is difficult to occur in the provided frequency range.[48,56] Meanwhile, Ru-SAS/SNC also exhibits superior tolerance ability to methanol crossover compared to Pt/C (Figure 2h). Above all, these electrochemical results strongly support that Ru-SAS/SNC can act as a competitive ORR catalyst to decrease or replace Pt usage.

Metal-Air Batteries Application. Owing to the fascinated electrochemical ORR activity and stability, the practicability of Ru-SAS/SNC as air cathodes in various types of metal-air (Zn-air, Al-air, and Li-O_2) batteries was verified in home-made energy conversion devices. Figure 3a shows the schematic setup of as-constructed Zn-air batteries with a zinc metal plate as anode and 6.0 M KOH as electrolyte. From the discharge polarization curves and power density plots for the Zn-Air battery (Figure 3b), we can see that the Ru-SAS/SNC-based battery exhibits a higher discharging voltage plateau with a maximum power density close to 229 mW cm^{-2}, which outperforms the Pt/C counterpart (175 mW cm^{-2}) as well as recently reported different categories of catalysts for primary Zn-air batteries.[29] Furthermore, the Ru-SAS/SNC-based Zn-air battery can deliver a higher open-circuit voltage of 1.52 V compared with the Pt/C-based battery (Figure 3c), suggesting a higher output voltage for the battery when using Ru-SAS/SNC as the cathode catalyst. According to the long-term discharge profile at 10 mA cm^{-2} (Figure S27), the discharge specific capacity (by normalized to the weight of zinc consumption) of the Ru-SAS/SNC-based battery could reach 728 mA h g_{Zn}^{-1}, corresponding to a high energy density of 925 Wh kg_{Zn}^{-1}, which is greatly larger than that of Pt/C (673 mA h g_{Zn}^{-1}) (Figure 3d). Ru-SAS/SNC (or Pt/C) was thereafter coupled with an oxygen-evolution catalyst (*i.e.*, RuO_2) to examine the galvanostatic discharge/charge cycling life of the Zn-air batteries. As displayed in Figure 3e, unlike the Pt/C-based battery with obvious voltage change, Ru-SAS/SNC-based Zn-air battery delivers a lower charge-discharge voltage gap and shows excellent stability in the discharge voltage from the initial potential (1.203 V) to the final one (1.195 V) after 270 h (810 cycles) of continuous operation, implying the great promise of Ru-SAS/SNC as the ORR catalyst for Zn-air batteries.

Similarly, Al-air batteries were assembled with Ru-SAS/SNC (or Pt/C) as the air-cathode, Al foil as the anode, and 0.1 M KOH as the electrolyte.[57,58] As shown in Figure S28, at a voltage of 0.566 V, the Al-air battery based on Ru-SAS/SNC presents a high current density of 74.67 mA cm^{-2} with the maximum power density of 42.12 mW cm^{-2}, which is superior to the commercial Pt/C-based battery (32.60 mW cm^{-2}). In addition, Ru-SAS/SNC produces a higher open-circuit voltage of ~1.49 V than the Pt/C electrode (~1.33 V). Further performance improvement of the Al-air battery can be achieved by electrolyte optimization and anode protection.[59,60] To further explore the feasibility of Ru-SAS/SNC as the cathode catalyst in Li-O_2 batteries, standard 2032-type coin cells (Figure S29a) were assembled for electrochemical tests in an O_2-filled glove box.[61,62] As expected, Ru-SAS/SNC displays improved performance in non-aqueous Li-O_2 batteries in comparison to commercial Pt/C (Figure S29b). In the first galvanostatic discharge profile measured at a current density of 200 mA g^{-1} and a limited capacity of 1000 mAh g^{-1}, Ru-SAS/SNC cathode demonstrates a much higher discharge potential with smaller polarization than Pt/C, indicating the efficient kinetics of Li_2O_2 formation.[62] Furthermore, the ORR process participated on Ru-SAS/SNC cathode delivers a less-steep constant voltage platform in the whole capacity range, suggesting the formation of Li_2O_2 at a relatively steady reaction rate.[63] The galvanostatic discharge pattern of Ru-SAS/SNC-based battery at a higher current density of 400 mA g^{-1} and a larger limited capacity of 2000 mAh g^{-1} was also recorded, in which the Ru-SAS/SNC catalytic electrode still shows smaller polarization, indicating the excellent rate capability of Ru-SAS/SNC cathode. Overall, Ru-SAS/SNC holds striking potentials in serving as an alternative to Pt/C in the practical metal-air battery systems.

ORR Catalytic Mechanism of Ru-SAS/SNC. To explore the underlying origin of catalytic behaviors of Ru active sites as well as the interaction mechanism of reaction intermediates, theoretical investigations in terms of intrinsic $4e^-$ ORR activity and electronic configuration were conducted based on DFT calculations. Firstly, we evaluated the binding energies (E_b) for the two structures of RuN_4-S (S bonded to N atoms in the second shell) and RuN_3S (S directly bonded to the central Ru atoms in the first shell). As shown in Table S6, E_b of the RuN_4-S configuration (-2.36 eV) is significantly more negative than that of the RuN_3S configuration (0.42 eV), which means that RuN_4-S coordination is more thermodynamically favorable. In the free energy diagram (Figure 4a), three oxygen-involved intermediates (*i.e.*, OOH^*, O^* and OH^*) were attached to Ru single-atomic-sites in our models of RuN_4 and RuN_4-S moieties, which were generated in succession according to the associative mechanism with incremental addition of molecular H_2O and electrons to form four OH^- in the end. All the intermediates on RuN_4-S have weaker binding energy, namely are more thermal-neutral, compared to those on RuN_4 at the electrode potential U_{RHE} = 1.23 V, suggesting more favorable oxygen intermediates adsorption on RuN_4-S sites.[31,46] In addition, at U_{RHE} = 1.23 V, the final electrochemical step, which is correlated with the OH^* binding, is verified to be the rate-determining step for both Ru-SAS/SNC and Ru-SAS/NC. On inornate RuN_4, the OH^* reduction was endothermic by 1.37 eV, suggesting that Ru-SAS/NC has relatively

strong adsorption for OH^*, which retards the removal of OH^* and the formation of OH^-. Whereas, the OH^* binding energy of RuN_4-S sites in Ru-SAS/SNC is 1.01 eV, smaller than that of inornate RuN_4, which is conducive to weakening the OH^* binding and enhancing the reaction kinetics in Ru-SAS/SNC.[64] Therefore, we can deduce that introduction of Ru-N-S coordination in the carbon matrix can optimize the adsorption of oxygen species and further boost the ORR activity, which coincides with the experimental result.

Crystal orbitals overlap population (COOP) method based on overlap-population-weighted densities-of-states, derived from identification of the interaction between Ru *d* orbitals and O *p* orbitals (Figure S30 and S31), was further established to extract the bonding information.[65,66] Therein, bonding and antibonding interactions typically appear as positive and negative COOP values, respectively. Zero COOP represents the nonbonding interactions.[65] As shown in Figure 4b and 4c, the energy (Y-axial value) position corresponding to the intersections at COOP = 0 of RuN_4-S moiety is relatively lower than that of RuN_4 moiety, manifesting the existence of more antibonding orbitals after O^* adsorption in RuN_4-S moiety. This could weaken the strong bonding of oxygen intermediates, resulting in the fast detachment of OH^* and boosted ORR performance of Ru centers. Due to the high correlation between the d-band center and metal-adsorbate interaction, the electronic structure of Ru centers, especially the density of states (DOS) was examined thereon (Figure 4d). The RuN_4-S units in Ru-SAS/SNC present a lower d-band center in comparison with Ru-SAS/NC (-0.95 eV over -0.15 eV), where the decrease of intermediates' adsorption free energy contributes to the increased ORR activity of Ru-SAS/SNC. The downshift of Ru d-band in Ru-SAS/SNC is probably ascribed to the deteriorated electron transfer from the Ru center to the electron-withdrawing N atoms in connection with S atoms.

Bader charge analysis (Figure 4e) further reveals that the electron donation from the surrounding N-S coordination can make the chemical valence of metal center Ru^{x+} of Ru-SAS/SNC less positive, resulting in a decreased adhesive strength with OH^*. Additionally, OH^* binding energy decreases as the Bader charge of the single-atom Ru increases, illustrating that Ru-SAS/SNC has better oxygen reduction catalytic activity over the Ru-SAS/NC. The charge density difference of Ru and S atoms was further investigated separately to distinguish the charge transfer circumstance of RuN_4-S moiety. In specific, when S atoms were selected as the object, electrons will transfer from S to N and further migrate to Ru central atoms, which causes a distinct augment of charge density on the Ru site (Figure 4f). Likewise, it can be exactly found that Ru is more apt to acquire electrons (Figure 4g). Thus, RuN_4-S moiety with S anions in the second coordination shell of Ru center is more favorable to weaken the adsorption of OOH^*, O^*, and OH^* on Ru centers relative to the single RuN_4 moiety. This observation is consistent with previous reports that anchoring anions in the second shell of TM_{3d}-N-C catalysts that are strongly bonded to intermediates, such as Fe-N_4 and Mn-N_4, can facilitate the ORR kinetics.[28,29,31,32]

CONCLUSIONS

In summary, we demonstrate that modulating the Ru-N-C catalyst through S-anion coordination at the second shell of Ru centers is effective to optimize the electronic structure and thereon ORR energetics and kinetics. The resultant catalyst manifests high ORR catalytic activity and glorious long-term stability. Experiment investigations and theoretical calculations reveal that the enhanced ORR performance is ascribed to the progressive charge densities of Ru centers and the low energy barrier of the ORR intermediates at RuN_4-S sites. This atomic-territory anion-coordination engineering strategy could provide a general approach to improve the ORR performance for a host of emerging M-N-C electrocatalysts.

ASSOCIATED CONTENT

Supporting Information. This material is available free of charge via the Internet at http://pubs.acs.org.

Experimental section, Detailed calculation modeling XRD patterns, Raman, XPS, XANES and EXAFS spectra, SEM and TEM images, N_2 adsorption-desorption isotherm curves, ICP-MS analysis, ORR, Al-air and Li-air measurements, a summary of recently reported single-atom ORR catalysts (PDF)

AUTHOR INFORMATION

Corresponding Author

* E-mail: huolinx@uci.edu (H. L. Xin)

Author Contributions

# Jiayi Qin and Hui Liu contributed equally to this work. All authors have given approval to the final version of the manuscript.

Notes

The authors declare no competing financial interest.

ACKNOWLEDGMENT

This work was supported by the National Science Foundation under award number CHE-1900401 and the startup funding of H.L.X. The authors acknowledge the use of facilities and instrumentation at the UC Irvine Materials Research Institute (IMRI), which is supported in part by the National Science Foundation through the UC Irvine Materials Research Science and Engineering Center (DMR-2011967). XPS was performed using instrumentation funded in part by the National Science Foundation Major Research Instrumentation Program under grant no. CHE-1338173. This research used 7-BM of the National Synchrotron Light Source II, a U.S. Department of Energy (DOE) Office of Science User Facility operated for the DOE Office of Science by Brookhaven National Laboratory under Contract No. DE-SC0012704. We would like to thank Dr. Lu Ma and Dr. Steven Ehrlich for their support at the 7-BM beamline.

REFERENCES

(1) Tian, X.; Zhao, X.; Su, Y.-Q.; Wang, L.; Wang, H.; Dang, D.; Chi, B.; Liu, H.; Hensen, E. J.; Lou, X. W. D., Engineering bunched Pt-Ni alloy nanocages for efficient oxygen reduction in practical fuel cells. *Science* **2019**, *366* (6467), 850-856.

(2) Jiang, K.; Zhao, D.; Guo, S.; Zhang, X.; Zhu, X.; Guo, J.; Lu, G.; Huang, X., Efficient oxygen reduction catalysis by subnanometer Pt alloy nanowires. *Sci. Adv.* **2017**, *3* (2), e1601705.

(3) Kodama, K.; Nagai, T.; Kuwaki, A.; Jinnouchi, R.; Morimoto, Y., Challenges in applying highly active Pt-based nanostructured catalysts for oxygen reduction reactions to fuel cell vehicles. *Nat. Nanotechnol.* **2021**, *16* (2), 140-147.

(4) Yuan, Y.; Wang, J.; Adimi, S.; Shen, H.; Thomas, T.; Ma, R.; Attfield, J. P.; Yang, M., Zirconium nitride catalysts surpass platinum for oxygen reduction. *Nat. Mater.* **2020**, *19* (3), 282-286.

(5) Xia, W.; Mahmood, A.; Liang, Z.; Zou, R.; Guo, S., Earth-

Abundant Nanomaterials for Oxygen Reduction. *Angew. Chem. Int. Ed.* **2016**, *55* (8), 2650-76.

(6) Xue, L.; Li, Y.; Liu, X.; Liu, Q.; Shang, J.; Duan, H.; Dai, L.; Shui, J., Zigzag carbon as efficient and stable oxygen reduction electrocatalyst for proton exchange membrane fuel cells. *Nat. Commun.* **2018**, *9* (1), 3819.

(7) Li, J.; Chen, M.; Cullen, D. A.; Hwang, S.; Wang, M.; Li, B.; Liu, K.; Karakalos, S.; Lucero, M.; Zhang, H.; Lei, C.; Xu, H.; Sterbinsky, G. E.; Feng, Z.; Su, D.; More, K. L.; Wang, G.; Wang, Z.; Wu, G., Atomically dispersed manganese catalysts for oxygen reduction in proton-exchange membrane fuel cells. *Nat. Catal.* **2018**, *1* (12), 935-945.

(8) Li, Z.; Ji, S.; Liu, Y.; Cao, X.; Tian, S.; Chen, Y.; Niu, Z.; Li, Y., Well-Defined Materials for Heterogeneous Catalysis: From Nanoparticles to Isolated Single-Atom Sites. *Chem. Rev.* **2020**, *120* (2), 623-682.

(9) Wang, A.; Li, J.; Zhang, T., Heterogeneous single-atom catalysis. *Nat. Rev. Chem.* **2018**, *2* (6), 65-81.

(10) Chen, Z. Q.; Huang, A. J.; Yu, K.; Cui, T. T.; Zhuang, Z. W.; Liu, S. J.; Li, J. Z.; Tu, R. Y.; Sun, K. A.; Tan, X.; Zhang, J. Q.; Liu, D.; Zhang, Y.; Jiang, P.; Pan, Y.; Chen, C.; Peng, Q.; Li, Y. D., Fe_1N_4-O_1 site with axial Fe-O coordination for highly selective CO_2 reduction over a wide potential range. *Energy Environ. Sci.* **2021**, *14*, 3430-3437.

(11) Liu, C. H.; Wu, Y.; Sun, K. A.; Fang, J. J.; Huang, A. J.; Pan, Y.; Cheong, W.; Zhuang, Z. W.; Zhuang, Z. B.; Yuan, Q. H.; Xin, H. L.; Zhang, C.; Zhang, J. W.; Xiao, H.; Chen, C.; Li, Y. D., Constructing FeN_4/graphitic nitrogen atomic interface for high-efficiency electrochemical CO_2 reduction over a broad potential window. *Chem* **2021**, 7 (5), 1297-1307.

(12) Wang, H. F.; Chen, L.; Pang, H.; Kaskel, S.; Xu, Q., MOF-derived electrocatalysts for oxygen reduction, oxygen evolution and hydrogen evolution reactions. *Chem. Soc. Rev.* **2020**, *49* (5), 1414-1448.

(13) Lu, X. F.; Xia, B. Y.; Zang, S. Q.; Lou, X. W. D., Metal-Organic Frameworks Based Electrocatalysts for the Oxygen Reduction Reaction. *Angew. Chem. Int. Ed.* **2020**, *59* (12), 4634-4650.

(14) Luo, E.; Zhang, H.; Wang, X.; Gao, L.; Gong, L.; Zhao, T.; Jin, Z.; Ge, J.; Jiang, Z.; Liu, C.; Xing, W., Single-Atom Cr-N_4 Sites Designed for Durable Oxygen Reduction Catalysis in Acid Media. *Angew. Chem. Int. Ed.* **2019**, *58* (36), 12469-12475.

(15) Yin, P.; Yao, T.; Wu, Y.; Zheng, L.; Lin, Y.; Liu, W.; Ju, H.; Zhu, J.; Hong, X.; Deng, Z.; Zhou, G.; Wei, S.; Li, Y., Single Cobalt Atoms with Precise N-Coordination as Superior Oxygen Reduction Reaction Catalysts. *Angew. Chem. Int. Ed.* **2016**, *55* (36), 10800-5.

(16) Zitolo, A.; Goellner, V.; Armel, V.; Sougrati, M. T.; Mineva, T.; Stievano, L.; Fonda, E.; Jaouen, F., Identification of catalytic sites for oxygen reduction in iron- and nitrogen-doped graphene materials. *Nat. Mater.* **2015**, *14* (9), 937-42.

(17) Wan, X.; Liu, X.; Li, Y.; Yu, R.; Zheng, L.; Yan, W.; Wang, H.; Xu, M.; Shui, J., Fe-N-C electrocatalyst with dense active sites and efficient mass transport for high-performance proton exchange membrane fuel cells. *Nat. Catal.* **2019**, *2* (3), 259-268.

(18) Xu, H.; Cheng, D.; Cao, D.; Zeng, X. C., A universal principle for a rational design of single-atom electrocatalysts. *Nat. Catal.* **2018**, *1* (5), 339-348.

(19) Pan, Y.; Zhang, C.; Liu, Z.; Chen, C.; Li, Y. D., Structural Regulation with Atomic-Level Precision: From Single-Atomic Site to Diatomic and Atomic Interface Catalysis. *Matter* **2020**, *2* (1), 78-110.

(20) Chen, G.; Liu, P.; Liao, Z.; Sun, F.; He, Y.; Zhong, H.; Zhang, T.; Zschech, E.; Chen, M.; Wu, G.; Zhang, J.; Feng, X., Zinc-Mediated Template Synthesis of Fe-N-C Electrocatalysts with Densely Accessible Fe-Nx Active Sites for Efficient Oxygen Reduction. *Adv. Mater.* **2020**, *32* (8), e1907399.

(21) Choi, C. H.; Lim, H.-K.; Chung, M. W.; Chon, G.; Ranjbar Sahraie, N.; Altin, A.; Sougrati, M.-T.; Stievano, L.; Oh, H. S.; Park, E. S.; Luo, F.; Strasser, P.; Dražić, G.; Mayrhofer, K. J. J.; Kim, H.; Jaouen, F., The Achilles' heel of iron-based catalysts during oxygen reduction in an acidic medium. *Energy Environ. Sci.* **2018**, *11* (11), 3176-3182.

(22) Wang, X. X.; Cullen, D. A.; Pan, Y. T.; Hwang, S.; Wang, M.; Feng, Z.; Wang, J.; Engelhard, M. H.; Zhang, H.; He, Y.; Shao, Y.; Su, D.; More, K. L.; Spendelow, J. S.; Wu, G., Nitrogen-Coordinated Single Cobalt Atom Catalysts for Oxygen Reduction in Proton Exchange Membrane Fuel Cells. *Adv. Mater.* **2018**, *30* (11), 1706758.

(23) Xiao, M.; Zhu, J.; Li, G.; Li, N.; Li, S.; Cano, Z. P.; Ma, L.; Cui, P.; Xu, P.; Jiang, G., A single-atom iridium heterogeneous catalyst in oxygen reduction reaction. *Angew. Chem. Int. Ed.* **2019**, *58* (28), 9640-9645.

(24) Sugawara, T.; Kawashima, N.; Murakami, T. N. Kinetic Study of Nafion Degradation by Fenton Reaction. J. Power Sources **2011**, *196*(5), 2615-2620.

(25) Xiao, M.; Gao, L.; Wang, Y.; Wang, X.; Zhu, J.; Jin, Z.; Liu, C.; Chen, H.; Li, G.; Ge, J.; He, Q.; Wu, Z.; Chen, Z.; Xing, W., Engineering Energy Level of Metal Center: Ru Single-Atom Site for Efficient and Durable Oxygen Reduction Catalysis. *J. Am. Chem. Soc.* **2019**, *141* (50), 19800-19806.

(26) Zhang, C.; Sha, J.; Fei, H.; Liu, M.; Yazdi, S.; Zhang, J.; Zhong, Q.; Zou, X.; Zhao, N.; Yu, H.; Jiang, Z.; Ringe, E.; Yakobson, B. I.; Dong, J.; Chen, D.; Tour, J. M., Single-Atomic Ruthenium Catalytic Sites on Nitrogen-Doped Graphene for Oxygen Reduction Reaction in Acidic Medium. *ACS Nano* **2017**, *11* (7), 6930-6941.

(27) Mun, Y.; Lee, S.; Kim, K.; Kim, S.; Lee, S.; Han, J. W.; Lee, J., Versatile Strategy for Tuning ORR Activity of a Single Fe-N_4 Site by Controlling Electron-Withdrawing/Donating Properties of a Carbon Plane. *J. Am. Chem. Soc.* **2019**, *141* (15), 6254-6262.

(28) Zhang, J.; Zhao, Y.; Chen, C.; Huang, Y. C.; Dong, C. L.; Chen, C. J.; Liu, R. S.; Wang, C.; Yan, K.; Li, Y.; Wang, G., Tuning the Coordination Environment in Single-Atom Catalysts to Achieve Highly Efficient Oxygen Reduction Reactions. *J. Am. Chem. Soc.* **2019**, *141* (51), 20118-20126.

(29) Shang, H.; Zhou, X.; Dong, J.; Li, A.; Zhao, X.; Liu, Q.; Lin, Y.; Pei, J.; Li, Z.; Jiang, Z.; Zhou, D.; Zheng, L.; Wang, Y.; Zhou, J.; Yang, Z.; Cao, R.; Sarangi, R.; Sun, T.; Yang, X.; Zheng, X.; Yan, W.; Zhuang, Z.; Li, J.; Chen, W.; Wang, D.; Zhang, J.; Li, Y., Engineering unsymmetrically coordinated Cu-S_1N_3 single atom sites with enhanced oxygen reduction activity. *Nat Commun.* **2020**, *11* (1), 3049.

(30) Shen, H.; Gracia-Espino, E.; Ma, J.; Zang, K.; Luo, J.; Wang, L.; Gao, S.; Mamat, X.; Hu, G.; Wagberg, T.; Guo, S., Synergistic Effects between Atomically Dispersed Fe-N-C and C-S-C for the Oxygen Reduction Reaction in Acidic Media. *Angew. Chem. Int. Ed.* **2017**, *56* (44), 13800-13804.

(31) Guo, L.; Hwang, S.; Li, B.; Yang, F.; Wang, M.; Chen, M.; Yang, X.; Karakalos, S. G.; Cullen, D. A.; Feng, Z., Promoting Atomically Dispersed MnN_4 Sites via Sulfur Doping for Oxygen Reduction: Unveiling Intrinsic Activity and Degradation in Fuel Cells. *ACS nano* **2021**, *15* (4), 6886-6899.

(32) Chen, Y.; Ji, S.; Zhao, S.; Chen, W.; Dong, J.; Cheong, W. C.; Shen, R.; Wen, X.; Zheng, L.; Rykov, A. I.; Cai, S.; Tang, H.; Zhuang, Z.; Chen, C.; Peng, Q.; Wang, D.; Li, Y., Enhanced oxygen reduction with single-atomic-site iron catalysts for a zinc-air battery and hydrogen-air fuel cell. *Nat Commun.* **2018**, *9* (1), 5422.

(33) Hu, B. T.; Huang, A. J.; Zhang, X. J.; Chen, Z.; Tu, R. Y.; Zhu, W.; Zhuang, Z. B.; Chen, C.; Peng, Q.; Li, Y. D., Atomic Co/Ni dual sites with N/P-coordination as bifunctional oxygen electrocatalyst for rechargeable zinc-air batteries. *Nano Res.* **2021**, *14* (10), 3482-3488.

(34) Wan, J.; Zhao, Z.; Shang, H.; Peng, B.; Chen, W.; Pei, J.; Zheng, L.; Dong, J.; Cao, R.; Sarangi, R.; Jiang, Z.; Zhou, D.; Zhuang, Z.; Zhang, J.; Wang, D.; Li, Y., In Situ Phosphatizing of Triphenylphosphine Encapsulated within Metal-Organic Frameworks to Design Atomic Co_1-P_1N_3 Interfacial Structure for Promoting Catalytic Performance. *J. Am. Chem. Soc.* **2020**, *142* (18), 8431-8439.

(35) Qin, J.; Xi, C.; Zhang, R.; Liu, T.; Zou, P.; Wu, D.; Guo, Q.; Mao, J.; Xin, H.; Yang, J., Activating Edge-Mo of 2H-MoS_2 via Coordination with Pyridinic N-C for pH-Universal Hydrogen Evolution

Electrocatalysis. *ACS Catal.* **2021**, *11* (8), 4486-4497.

(36) Li, Z.; Chen, Y.; Ji, S.; Tang, Y.; Chen, W.; Li, A.; Zhao, J.; Xiong, Y.; Wu, Y.; Gong, Y.; Yao, T.; Liu, W.; Zheng, L.; Dong, J.; Wang, Y.; Zhuang, Z.; Xing, W.; He, C. T.; Peng, C.; Cheong, W. C.; Li, Q.; Zhang, M.; Chen, Z.; Fu, N.; Gao, X.; Zhu, W.; Wan, J.; Zhang, J.; Gu, L.; Wei, S.; Hu, P.; Luo, J.; Li, J.; Chen, C.; Peng, Q.; Duan, X.; Huang, Y.; Chen, X. M.; Wang, D.; Li, Y., Iridium single-atom catalyst on nitrogen-doped carbon for formic acid oxidation synthesized using a general host-guest strategy. *Nat. Chem.* **2020**, *12* (8), 764-772.

(37) Cao, L.; Luo, Q.; Chen, J.; Wang, L.; Lin, Y.; Wang, H.; Liu, X.; Shen, X.; Zhang, W.; Liu, W.; Qi, Z.; Jiang, Z.; Yang, J.; Yao, T., Dynamic oxygen adsorption on single-atomic Ruthenium catalyst with high performance for acidic oxygen evolution reaction. *Nat Commun.* **2019**, *10* (1), 4849.

(38) Xiong, Y.; Dong, J.; Huang, Z. Q.; Xin, P.; Chen, W.; Wang, Y.; Li, Z.; Jin, Z.; Xing, W.; Zhuang, Z.; Ye, J.; Wei, X.; Cao, R.; Gu, L.; Sun, S.; Zhuang, L.; Chen, X.; Yang, H.; Chen, C.; Peng, Q.; Chang, C. R.; Wang, D.; Li, Y., Single-atom Rh/N-doped carbon electrocatalyst for formic acid oxidation. *Nat. Nanotechnol.* **2020,** *15* (5), 390-397.

(39) Liu, W.; Zhang, L.; Liu, X.; Liu, X.; Yang, X.; Miao, S.; Wang, W.; Wang, A.; Zhang, T., Discriminating Catalytically Active FeNx Species of Atomically Dispersed Fe-N-C Catalyst for Selective Oxidation of the C-H Bond. *J. Am. Chem. Soc.* **2017**, *139* (31), 10790-10798.

(40) Kim, M.; Yoo, J. M.; Ahn, C. Y.; Jang, J. H.; Son, Y. J.; Shin, H.; Kang, J.; Kang, Y. S.; Yoo, S. J.; Lee, K. S., Rational Generation of Fe-Nx Active Sites in Fe-N-C Electrocatalysts Facilitated by Fe-N Coordinated Precursors for the Oxygen Reduction Reaction. *ChemCatChem* **2019**, *11* (24), 5982-5988.

(41) Li, J.; Zhang, Y.; Zhang, X.; Huang, J.; Han, J.; Zhang, Z.; Han, X.; Xu, P.; Song, B., S, N Dual-Doped Graphene-like Carbon Nanosheets as Efficient Oxygen Reduction Reaction Electrocatalysts. *ACS Appl. Mater. Interfaces* **2017**, *9* (1), 398-405.

(42) Sarangi, R.; Cho, J.; Nam, W.; Solomon, E. I., XAS and DFT investigation of mononuclear cobalt(III) peroxo complexes: electronic control of the geometric structure in CoO_2 versus NiO_2 systems. *Inorg. Chem.* **2011,** *50* (2), 614-620.

(43) Liu, X.; Liu, F.; Yu, J.; Xiong, G.; Zhao, L.; Sang, Y.; Zuo, S.; Zhang, J.; Liu, H.; Zhou, W., Charge Redistribution Caused by S,P Synergistically Active Ru Endows an Ultrahigh Hydrogen Evolution Activity of S-Doped RuP Embedded in N, P, S-Doped Carbon. *Adv. Sci.* **2020**, *7* (17), 2001526.

(44) Wang, Q.; Shang, L.; Sun-Waterhouse, D.; Zhang, T.; Waterhouse, G., Engineering local coordination environments and site densities for high-performance Fe-N-C oxygen reduction reaction electrocatalysis. *Adv. Energy Mater.* **2021**, 2100219.

(45) Tong, M.; Sun, F.; Xie, Y.; Wang, Y.; Yang, Y.; Tian, C.; Wang, L.; Fu, H., Operando Cooperated Catalytic Mechanism of Atomically Dispersed Cu-N_4 and Zn-N_4 for Promoting Oxygen Reduction Reaction. *Angew. Chem. Int. Ed.* **2021**, *60* (25), 14005-14012.

(46) Shao, C.; Wu, L.; Zhang, H.; Jiang, Q.; Xu, X.; Wang, Y.; Zhuang, S.; Chu, H.; Sun, L.; Ye, J., A Versatile Approach to Boost Oxygen Reduction of Fe-N_4 Sites by Controllably Incorporating Sulfur Functionality. *Adv. Funct. Mater.* **2021**, 2100833.

(47) Nie, Y.; Li, L.; Wei, Z., Recent advancements in Pt and Pt-free catalysts for oxygen reduction reaction. *Chem. Soc. Rev*. **2015**, *44*, 2168-2201.

(48) Shinozaki, K.; Zack, J.; Richards, R.; Pivovar, B.; Kocha, S., Oxygen Reduction Reaction Measurements on Platinum Electrocatalysts Utilizing Rotating Disk Electrode Technique: I. Impact of Impurities, Measurement Protocols and Applied Corrections. *J. Electrochem. Soc.* **2015**, *162* (10), F1144-F1158.

(49) Garsany, Y.; Baturina, O.; Swider-Lyons, K.; Kocha, S., Experimental Methods for Quantifying the Activity of Platinum Electrocatalysts for the Oxygen Reduction Reaction. *Anal. Chem.* **2010**, *82* (15), 6321-6328.

(50) Cao, Y.; Peng, H.; Chu, S.; Tang, Y.; Huang, C.; Wang, Z.; Liu, F.; Wu, J.; Shan, B.; Chen, R., Molten-salt-assisted thermal emitting method to transform bulk Fe_2O_3 into Fe single atom catalysts for oxygen reduction reaction in Zn-air battery. *Chem. Eng. J.* **2021**, *420*, 129713.

(51) Wei, X.; Song, S.; Wu, N.; Luo, X.; Zheng, L.; Jiao, L.; Wang, H.; Fang, Q.; Hu, L.; Gu, W., Synergistically enhanced single-atomic site Fe by Fe_3C@C for boosted oxygen reduction in neutral electrolyte. *Nano Energy* **2021,** *84*, 105840.

(52) Ding, R.; Liu, Y.; Rui, Z.; Li, J.; Liu, J.; Zou, Z., Facile grafting strategy synthesis of single-atom electrocatalyst with enhanced ORR performance. *Nano Res.* **2020**, *13* (6), 1519-1526.

(53) Wu, G.; Chung, H. T.; Nelson, M.; Artyushkova, K.; More, K. L.; Johnston, C. M.; Zelenay, P., Graphene-riched Co_9S_8-NC non-precious metal catalyst for oxygen reduction in alkaline media. *ECS Trans.* **2011**, *41* (1), 1709.

(54) Xiao, M.; Zhu, J.; Ma, L.; Jin, Z.; Ge, J.; Deng, X.; Hou, Y.; He, Q.; Li, J.; Jia, Q., Microporous framework induced synthesis of single-atom dispersed Fe-NC acidic ORR catalyst and its in situ reduced Fe-N_4 active site identification revealed by X-ray absorption spectroscopy. *ACS Catal.* **2018**, *8* (4), 2824-2832.

(55) Zhang, L.; Fischer, J.; Jia, Y.; Yan, X.; Xu, W.; Wang, X.; Chen, J.; Yang, D.; Liu, H.; Zhuang, L.; Hankel, M.; Searles, D. J.; Huang, K.; Feng, S.; Brown, C. L.; Yao, X., Coordination of Atomic Co-Pt Coupling Species at Carbon Defects as Active Sites for Oxygen Reduction Reaction. *J. Am. Chem. Soc.* **2018**, *140* (34), 10757-10763.

(56) Singh, R. K.; Devivaraprasad, R.; Kar, T.; Chakraborty, A.; Neergat, M., Electrochemical Impedance Spectroscopy of Oxygen Reduction Reaction (ORR) in a Rotating Disk Electrode Configuration: Effect of Ionomer Content and Carbon-Support. *J. Electrochem. Soc.* **2015**, *162* (6), F489-F498.

(57) Jiang, M.; Yang, J.; Ju, J.; Zhang, W.; He, L.; Zhang, J.; Fu, C.; Sun, B., Space-confined synthesis of CoNi nanoalloy in N-doped porous carbon frameworks as efficient oxygen reduction catalyst for neutral and alkaline aluminum-air batteries. *Energy Storage Mater.* **2020**, *27*, 96-108.

(58) Liu, Y.; Yang, L.; Xie, B.; Zhao, N.; Yang, L.; Zhan, F.; Pan, Q.; Han, J.; Wang, X.; Liu, J., Ultrathin Co_3O_4 nanosheet clusters anchored on nitrogen doped carbon nanotubes/3D graphene as binder-free cathodes for Al-air battery. *Chem. Eng. J.* **2020**, *381*, 122681.

(59) Wu, P.; Wu, S.; Sun, D.; Tang, Y.; Wang, H., A Review of Al Alloy Anodes for Al–Air Batteries in Neutral and Alkaline Aqueous Electrolytes. *Acta Metall. Sin. (Engl. Lett.)* **2021**, *34*, 309-320.

(60) Zhang, Z.; Zuo, C.; Liu, Z.; Yu, Y.; Zuo, Y.; Song, Y., All-solid-state Al-air batteries with polymer alkaline gel electrolyte. *J. Power Sources* **2014**, *251*, 470-475.

(61) Luo, M.; Zhao, Z.; Zhang, Y.; Sun, Y.; Xing, Y.; Lv, F.; Yang, Y.; Zhang, X.; Hwang, S.; Qin, Y., PdMo bimetallene for oxygen reduction catalysis. *Nature* **2019**, *574* (7776), 81-85.

(62) Wang, P.; Li, C.; Dong, S.; Ge, X.; Zhang, P.; Miao, X.; Wang, R.; Zhang, Z.; Yin, L., Hierarchical $NiCo_2S_4$@NiO core-shell heterostructures as catalytic cathode for long-life Li-O_2 batteries. *Adv. Energy Mater.* **2019**, *9* (24), 1900788.

(63) Han, J.; Guo, X.; Ito, Y.; Liu, P.; Hojo, D.; Aida, T.; Hirata, A.; Fujita, T.; Adschiri, T.; Zhou, H., Effect of Chemical Doping on Cathodic Performance of Bicontinuous Nanoporous Graphene for Li-O_2 Batteries. *Adv. Energy Mater.* **2016**, *6* (3), 1501870.

(64) Zheng, Y.; Yang, D.-S.; Kweun, J. M.; Li, C.; Tan, K.; Kong, F.; Liang, C.; Chabal, Y. J.; Kim, Y. Y.; Cho, M., Rational design of common transition metal-nitrogen-carbon catalysts for oxygen reduction reaction in fuel cells. *Nano Energy* **2016**, *30*, 443-449.

(65) Steinberg, S.; Dronskowski, R., The crystal orbital Hamilton population (COHP) method as a tool to visualize and analyze chemical bonding in intermetallic compounds. *Crystals* **2018**, *8* (5), 225.

(66) Grechnev, A.; Ahuja, R.; Eriksson, O., Balanced crystal orbital overlap population—a tool for analysing chemical bonds in solids. *J. Phys.: Condens. Matter* **2003,** *15* (45), 7751.

SYNOPSIS TOC (Word Style "SN_Synopsis_TOC"). If you are submitting your paper to a journal that requires a synopsis graphic and/or synopsis paragraph, see the Instructions for Authors on the journal's homepage for a description of what needs to be provided and for the size requirements of the artwork.

To format double-column figures, schemes, charts, and tables, use the following instructions:

Place the insertion point where you want to change the number of columns
From the **Insert** menu, choose **Break**
Under **Sections**, choose **Continuous**
Make sure the insertion point is in the new section. From the **Format** menu, choose **Columns**
In the **Number of Columns** box, type **1**
Choose the **OK** button

Now your page is set up so that figures, schemes, charts, and tables can span two columns. These must appear at the top of the page. Be sure to add another section break after the table and change it back to two columns with a spacing of 0.33 in.

Table 1. Example of a Double-Column Table

Column 1	Column 2	Column 3	Column 4	Column 5	Column 6	Column 7	Column 8

Authors are required to submit a graphic entry for the Table of Contents (TOC) that, in conjunction with the manuscript title, should give the reader a representative idea of one of the following: A key structure, reaction, equation, concept, or theorem, etc., that is discussed in the manuscript. Consult the journal's Instructions for Authors for TOC graphic specifications.

Insert Table of Contents artwork here